Soft Matter

ARTICLE TYPE

Cite this: DOI: 00.0000/xxxxxxxxxx

Flow transitions and length scales of a channel-confined active nematic

Abhik Samui,[a] Julia M. Yeomans [b] and Sumesh P. Thampi [c]

Received Date
Accepted Date

DOI: 00.0000/xxxxxxxxxx

We perform lattice Boltzmann simulations of an active nematic fluid confined in a two-dimensional channel to study the range of flow states that are stabilised by the confinement: unidirectional flow, oscillatory flow, the dancing state, localised active turbulence and fully-developed active turbulence. We analyse the flows in Fourier space, and measure a range of different length scales which describe the flows. We argue that the different states occur as a result of flow instabilities inherent to the system. As a consequence the characteristic length scale for oscillatory flow, the dancing state and localised active turbulence is set by the channel width. Fully-developed active turbulence occurs only when the channel width is larger than the intrinsic, active length scale of the bulk fluid. The results clarify why the activity number is a control parameter for the flow transitions.

1 Introduction

Active nematics are fluids that comprise anisotropic active entities that consume available energy and perform mechanical work. This energy throughput is often reflected as self propulsion of the active particles, they exert a stress field on the surrounding medium, thus maintaining the system in a non-equilibrium state[1–4]. Active nematics include a variety of biological systems such as bacterial suspensions[5–9], collections of cells[10–12], and microtubules and motor protein mixtures[13,14], and synthetic systems such as vibrating granular rods[15,16] and phoretic active particles[17]. Collective dynamics and long-range interactions in these materials manifest as many interesting and complex phenomena, among which active turbulence, a low Reynolds number turbulent-like flow, has drawn much attention in the recent past[6,18–20]. Experiments and simulations reveal that the flow structures of active turbulence exhibit a natural length scale, often referred to as the active length scale. The active length scale arises because of the competition between the destabilising effect of the active stresses and the elastic relaxation of the medium[21–23].

Since active turbulence is produced as a result of spontaneous flow transitions it offers possibilities for novel microfluidic applications using active systems. However, the very nature of the flow field, namely its chaotic behaviour and the lack of control, act as a hindrance to such applications. In this regard, confinement has been proposed as a way to control the turbulent flow structures produced by active nematics. This route is still far from success, but instead it has revealed interesting properties of active systems in confinement and opened up new research questions. For example, kinesin-microtubule mixtures in a two-dimensional circular confinement produce distinct flow states, ranging from net circular flows to active turbulence, depending upon the dimensions of the confinement[20,24,25]. Similarly, Xenopus egg extract shows cytoplasmic flow-like structure in droplets[26]. A kinesin-microtubule mixture on a deformable spherical lipid vesicle produces oscillating defect dynamics[27], on the surface of a toroidal droplet shows curvature-induced defect unbinding[28] and confined in a three-dimensional cylindrical or annular channel shows aspect-ratio driven flow transitions[29]. Likewise, various coherent flows are generated by bacterial suspensions in two-dimensional rectangular channels[9] and by microtubule-motor protein mixtures in two- and three-dimensional rectangular channels[29,30].

Despite several investigations[9,30–36], the emergence of different flow states or their structures in confined active nematics is not completely understood. Therefore, in this work, we analyse the fluid flows generated by an active nematic in both real and Fourier space. This allows us to demonstrate that the flow transitions observed in a two-dimensional, channel-confined active nematic result from instabilities intrinsic to the fluid and as a consequence, the characteristic length scale of different flow states is set by the channel width.

This paper is organised as follows: In section 2, we briefly discuss the governing equations that describe the dynamics of active nematics, and details of the simulations. Our results are presented in section 3. We first review the different flow states that an active nematic realizes in confinement, and then use several

[a] Department of Physics, Indian Institute of Technology Madras, Chennai 600036, India. E-mail: abhiks@physics.iitm.ac.in
[b] The Rudolf Peierls Centre for Theoretical Physics, Clarendon Laboratory, Parks Road, Oxford, OX1 3PU, UK. E-mail: julia.yeomans@physics.ox.ac.uk
[c] Department of Chemical Engineering, Indian Institute of Technology Madras, Chennai 600036, India. E-mail: sumesh@iitm.ac.in

different approaches to analyse the characteristic lengths exhibited by each of these flow states. We show that the different flow states arise from various flow instabilities inherent in the system, and discuss the activity number, the dimensionless variable that controls the flow transitions. Finally we summarise our results in section 4.

2 Computer simulations of active nematohydrodynamics

The dynamics of dense suspensions of active nematic constituents can be modelled in the framework of the hydrodynamic theory of liquid crystals[37–39] with additional physics incorporated to account for the activity of the system[40–42]. We use the continuum theory which describes the mass and momentum conservation equations of an incompressible suspension as

$$\nabla \cdot \mathbf{u} = 0, \tag{1}$$

$$\rho(\partial_t + \mathbf{u}\cdot\nabla)\mathbf{u} = \nabla\cdot\boldsymbol{\pi}^{tot} \tag{2}$$

where ρ is the density of the active fluid, $\mathbf{u}$ is the fluid velocity and $\boldsymbol{\pi}^{tot}$ is the total stress, the sum of three contributions[42], the viscous, elastic and active stresses. The microstructural evolution in the fluid is described by[37,43]

$$(\partial_t + \mathbf{u}\cdot\nabla)\mathbf{Q} - \mathbf{S} = \Gamma\mathbf{H} \tag{3}$$

where $\mathbf{Q}$ is a tensor order parameter which describes the orientational order of the active constituents, $\mathbf{S}$ is a generalised advection term, Γ is the orientational diffusivity and $\mathbf{H}$ is the molecular potential field associated with an elastic free energy. The passive system is in the isotropic phase, and any nematic ordering is due to the activity[44]. The active stress, the hyrodynamic stress field generated by the active constituents is taken to be proportional to $\mathbf{Q}$. Thus, $\boldsymbol{\pi}^{active} = -\zeta\mathbf{Q}$ where ζ is the activity coefficient, and $\zeta < 0$ for contractile systems and $\zeta > 0$ for extensile systems[40]. Full details of the continuum description can be found in several papers[33,42,45,46] and are reproduced in section S1 in the SI for convenience.

The governing equations are solved in a rectangular domain using a hybrid lattice Boltzmann algorithm[42,45]. This method involves sequential temporal updates using a lattice Boltzmann method for the Navier-Stokes equations (1) and (2) and a method of lines for the $\mathbf{Q}$ evolution equation (3). The grid and time resolutions are chosen as unity following the usual framework of lattice Boltzmann approaches[47]. Thus, all the parameters are reported in lattice units which can be re-scaled to match the experimental results[46,48,49].

The simulations are performed in a channel of length $l = 200$ in the x-direction, unless otherwise stated. (See Fig. S1 for a schematic of the two dimensional channel in SI.) No-slip boundary conditions for the velocity field and a strong homogeneous anchoring condition for the director field are applied on the channel walls. Though the mathematical framework described above is in three dimensions, we have imposed periodic boundary conditions in the direction perpendicular to the plane of the channel in order to carry out the study in a two dimensions. The open sides of the channel are also assumed to be periodic. Other parameters used are, $\Gamma = 0.34$, $\rho = 1.0$, alignment parameter $\lambda = 0.4$ and viscosity $\eta = 0.667$, and the active system is taken to be extensile ($\zeta > 0$). The activity parameter ζ, elastic constant K and channel width w are varied in the simulations. For all simulations, we have chosen the initial fluid velocity as zero and initial $\mathbf{Q}$ tensor to correspond to a randomly oriented director field with a magnitude of the order parameter, $q \approx 10^{-10}$.

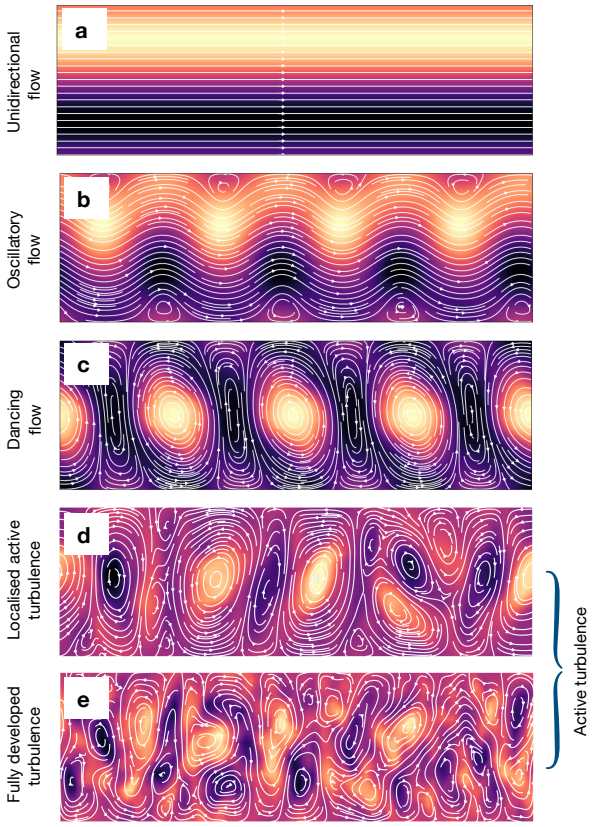

Fig. 1 Steady state flow of the five distinct flow states observed in channel-confined active nematics: (a) unidirectional ($\zeta = 0.0024$), (b) oscillatory ($\zeta = 0.0029$), (c) dancing ($\zeta = 0.01$), (d) localised active turbulence ($\zeta = 0.0245$) and (e) fully-developed active turbulence ($\zeta = 0.08$). In the plots the continuous lines are streamlines and the colour map shows the vorticity field (dark magenta for clockwise to golden yellow for anticlockwise). In all cases, simulations are performed in a channel of size 100×20.

3 Results

3.1 Flow states of an active nematic in a 2D channel

We summarise the sequence of flow states reported in 2D channel-confined extensile active nematics as the activity is increased, namely unidirectional, oscillatory, dancing and active turbulent flows. The steady state flow fields corresponding to these states are shown in Fig. 1.

Unidirectional flow: In the absence of activity ($\zeta = 0$) the director field remains isotropic, and no flows develop. But if the activ-

ity is increased, then at a critical activity[50] spontaneous symmetry breaking occurs and the active nematic flows. The corresponding flow state is unidirectional since $u_x \neq 0$ but $u_y = 0$ everywhere. As shown in Fig. 1(a) the velocity is symmetric with respect to the channel centre line and the vorticity field has opposite signs (sense of rotation) in the upper and lower half of the channel.

Oscillatory flow: With further increase in activity, different flow states ensue. The first among these is oscillatory flow, shown in Fig. 1(b). In this state, streamlines resemble travelling waves. Further, small circulations develop near the walls at the crest and trough of the waves. These are a consequence of accommodating the sinusoidal structure of the waves between planar walls. The corresponding vorticity field also has a wavy pattern, but of opposite signs in the upper and lower halves of the channel. Moreover the vorticity field exhibits local regions of stronger vorticity at the positions of the crests and troughs of the waves, staggered across the channel center line.

Dancing flow: At higher activities, the streamlines close in on themselves resulting in the appearance of a line of alternating clockwise and anticlockwise vortices along the channel as shown in Fig. 1(c). Hence, there is now no net flow along the channel length. Moreover, this regular arrangement of alternating vortices oscillates in time. This flow state acquires its name from the fact that there are $+1/2$ topological defects in the director field within the mid-region of the channel, and alternate $+1/2$ defects move continuously along the channel in opposite directions resulting in exchanges of pairs reminiscent of a Ceilidh dance[33].

Active turbulence: With further increase in activity, the regularity of the vortex structure disappears and the flow becomes turbulent. We distinguish two different flow regions of active turbulence, which we will term localised active turbulence and fully-developed active turbulence. These are shown in Fig. 1(d) and Fig. 1(e) respectively.

In the first case, *i.e.* in the region of localised active turbulence, disordered patches, or clusters, of local active turbulence are observed. These regions, called active puffs[51], are created spontaneously, persist in time and then decay[51]. Hence, regions of vortex lattice and active puffs coexist. The higher the activity, the longer the active puffs exist before they decay.

As the activity is increased further, the region occupied by active puffs grows replacing the vortex lattices and finally occupying the entire channel. In this state, the flow pattern appears chaotic as shown in Fig. 1(e). Vortices of different sizes continuously form and disappear throughout the channel. This state of turbulent-like flow, which occurs despite being at very low Reynolds number, is known as fully-developed active turbulence[6,18,51]. It has been demonstrated that the corresponding director field is equally chaotic with $+1/2$ and $-1/2$ defects continuously created and annihilated[45].

3.2 Flow states interpreted as excitation of waves

Fig. 1 shows that the transition from unidirectional to oscillatory flow occurs with the appearance of wave-like structures. To understand the formation and consequent growth of these waves, we perform a one-dimensional discrete Fourier transform (see

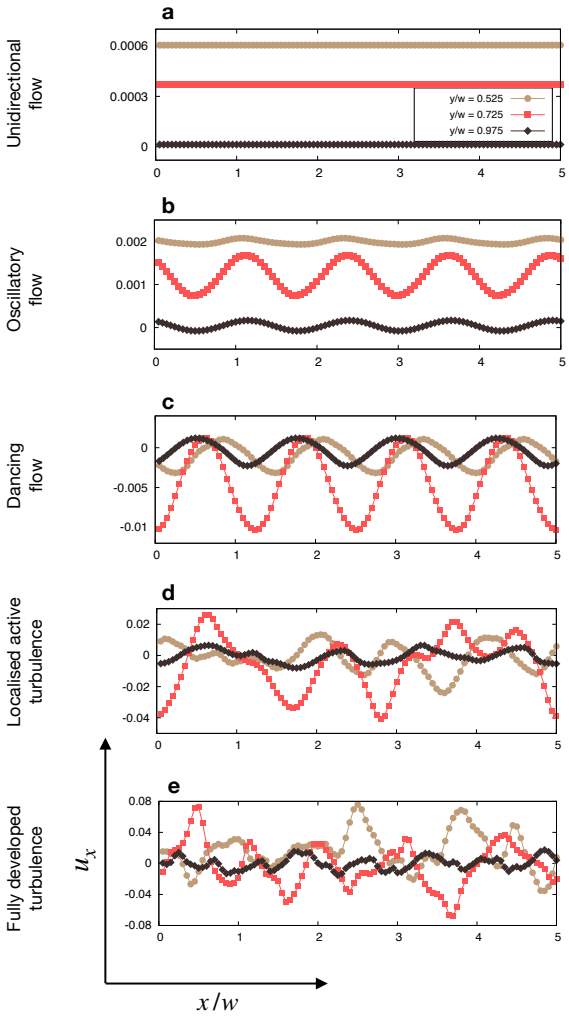

Fig. 2 Spatial variation in u_x along the channel length for all the flow states shown in Fig. 1. The three data sets in each plot are for 3 different y locations: $y/w = 0.525$ is close to the channel center line and $y/w = 0.975$ is close to the wall (as depicted in Fig. S1). In the plots, only y locations from the upper half of the channel are presented as the flow field is symmetric about the channel centre.

section S2 in SI) of the x- and y- components of the velocity field, u_x and u_y, and of the vorticity field, ω_z. The results are illustrated in Fig. 2, which shows the instantaneous velocity u_x along the channel length, x, and in Fig. 3 which shows the power spectra of $u_x(x)$.

At low activity there is no flow, the velocity field is zero, and correspondingly the power spectrum is empty in the $k-\zeta$ space, as shown in Fig. 3. For unidirectional flows, u_x is only a function of y, with the velocity being maximum at the channel centre line and reducing to zero at the no-slip walls of the channel (see Fig. 2(a)). Correspondingly, the amplitude of the Fourier modes $a_k = 0$ for all $k \neq 0$, indicating the absence of any wave-like structures in the unidirectional flow state, and the power spectrum is empty.

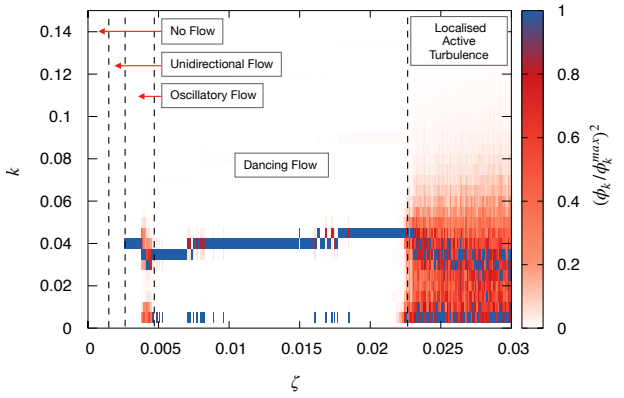

Fig. 3 Fourier amplitudes of $u_x(x)$, for $k \neq 0$ modes, in the $k-\zeta$ plane. The colour bar represents the power $(\phi_k)^2$ of each mode (see section S2.2 in SI), normalised by the respective maximum $(\phi_k^{max})^2$ (i.e, ϕ_k^{max} at the same ζ). Due to the discrete nature of the wave number, each point on this plot is shown as a small, rectangle of colour. Vertical dashed lines demarcate various flow states.

The first non-zero Fourier mode is found in the oscillatory flow state. As shown in Fig. 2(b), u_x at each value of y/w is a function of x as well, with the variation appearing similar to that of a sinusoidal wave. The mean value of u_x gradually decreases from the channel center towards the channel wall, as for the case of a unidirectional flow. However, the amplitude of oscillations is larger for the intermediate values of y, i.e, for $(y/w = 0.725)$ than at the channel center or near to the wall. Interestingly, there is no phase lag between the waves at various y locations. The corresponding spectrum in Fig. 3, which gives the normalised, spatio-temporal average of the Fourier amplitudes a_k, shows that only a single mode is present illustrating the truly sinusoidal nature of $u_x(x)$ in the oscillatory flow state. The excitation of just a single mode continues to hold for a range of ζ. Further increases in activity excite multiple modes, and the spectra are dispersed in k space. However, the flow remains oscillatory although with a velocity field that is more irregular. These states have a net flow $(\langle u_x \rangle \neq 0)$ along the channel length which distinguish them from turbulent flow.

The instantaneous velocities $u_x(x)$ at the three different y locations corresponding to the dancing state are shown in Fig. 2(c). It can be seen that $u_x(x)$ is a sinusoidal function, similar to that for the oscillatory flow, but with the following important distinctions: (i) Both the mean velocity and the amplitude of oscillations are maximum at intermediate values of y and they reduce towards the channel centre and towards the channel walls. (ii) The instantaneous velocity profiles $u_x(x)$ at different y locations do not have the same phase. In the snapshot shown in Fig. 1(c) the clockwise vortices are weaker, and therefore $u_x(x)$ is predominantly negative. The vortices show a characteristic tilt reminiscent of the underlying shear flow associated with the dominant, anticlockwise vortex in Fig. 1(c), and hence the waves representing $u_x(x)$ at different y locations in Fig. 2(c) show a phase shift.

Similar to the findings in the oscillatory state the power spectrum for the dancing state in Fig. 3 shows that normally a single mode is excited. This single mode indicates that the flow field associated with the dancing state has, as expected, a unique characteristic length, the distance between two co-rotating vortices. However, it is interesting to note in Fig. 3 that, occasionally, modes whose wavelength is comparable to the channel length $(k \approx 0)$ appear in the dancing state. This is because distorted vortex lattices, which lead to an intermittent net flow, can appear in these flow states. Barring this occasional appearance, only a single mode describes both the oscillatory and the dancing flow.

This picture changes at higher values of activity, when the system reaches the localised active turbulence and fully-developed active turbulent states. For these two states Fig. 2(d) and Fig. 2(e) show that the $u_x(x)$ at all three y locations are very irregular indicating the turbulent nature of the underlying flow field. Similar to dancing flows the magnitude of u_x and the amplitude of its fluctuations are largest at $y/w = 0.725$. More importantly, these velocity profiles $u_x(x)$ suggest that multiple waves of different wave numbers are excited in the two turbulent states. This is confirmed in the Fourier spectra shown in Fig. 3 where several modes show nonzero amplitude. Interestingly, the spectral distribution does not have a single peak, but rather the spectra are bimodal (see section S3 in the SI for a detailed analysis), with the two dominant wave numbers at $kw \approx 0$ and $kw \approx 1.0$. But these peaks are not pronounced, instead the modes in the neighbourhood of the peaks also carry significant power, ϕ_k. It is also interesting to note that one of the peaks occurs at $k \approx 0$, which suggests that some of the dominant waves in u_x have wavelengths comparable to the channel length. A similar analysis was carried out for the transverse component of the velocity field $u_y(x)$ and the vorticity field $\omega_z(x)$. We found that the power spectra for both $u_y(x)$ and $\omega_z(x)$ (shown in Fig. S3(b,c) in the SI) are also similar to Fig. 3. The power spectra for fully developed active turbulence are also shown in Fig. S3.

An important observation to be made from Fig. 3 is that the wave number k at which the single peak appears in both oscillatory and dancing flows, and the wavelength corresponding to the most dominant mode with larger k for localised active turbulent flows remains approximately constant, independent of activity. This is perhaps surprising, considering that ζ changes over a large range and it is this change that drives the transitions between flow states. To gain more insight into the flow transitions, we next compare results for different real-space length scales.

3.3 The characteristic length scales of channel-confined active nematic flows

Fig. 4(a) shows the characteristic lengths $L_F^{u_x}$ (black), $L_F^{u_y}$ (red) and $L_F^{\omega_z}$ (yellow) corresponding to dominant Fourier mode of u_x, u_y and ω_z respectively as a function of activity (see the SI, section S2.2, for the exact definitions). In the oscillatory and dancing regimes (denoted (*ii*) and (*iii*) in the Figure) these length scales are approximately the same and close to the channel width in agreement with the results in k-space. The few outliers for $L_F^{u_x}$ in region (*iii*) correspond to the occasional instances of net flow.

In the active turbulent flow regime (only localised active turbulence is shown here, marked as (*iv*)), however, the character-

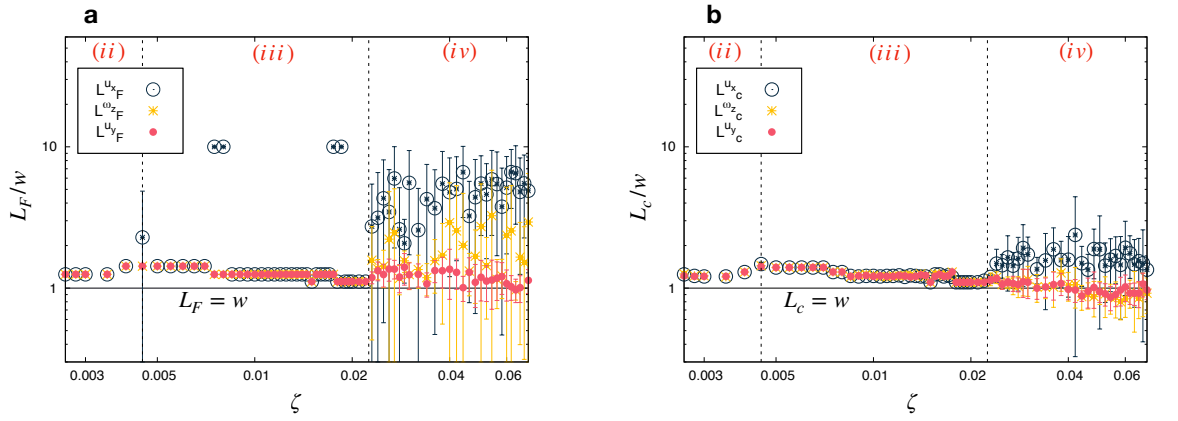

Fig. 4 Characteristic length scales (a) L_F and (b) L_c corresponding to variation in activity (ζ) for $K = 0.01$, $l = 200$ and $w = 20$. In the left panel $L_F^{u_x}$ (black), $L_F^{u_y}$ (red) and $L_F^{\omega_z}$ (yellow) are extracted from Fourier amplitudes. On the right panel, $L_c^{u_x}$ (black), $L_c^{u_y}$ (red) and $L_c^{\omega_z}$ (yellow) are from correlation functions. L_F and L_c are non-dimensionalised by the channel width w. The black dashed lines demarcate different flow states, namely (ii), (iii) and (iv) indicate oscillatory flow, dancing flow and localised active turbulence respectively.

istic length scales have different means and standard deviations. Among the three measures, $L_F^{u_x}$ is highest, and it shows large fluctuations about its mean value. This reflects the Fourier transform data which indicated a range of length scales with mild peaks at wavelengths w and l (see also Fig. S2(a) in SI). With increase in activity the mean value of $L_F^{u_x}$ drifts towards the channel length ($L_F^{u_x} \approx 10w$ in the case illustrated in Fig. 4(a)). This may be an indication of the presence of fluid jets along the channel in the localised active turbulent flow state. The length scale calculated from the Fourier transform of the vorticity field, $L_F^{\omega_z}$, can also attain values close to channel length, but this occurs less frequently than for $L_F^{u_x}$. Hence its mean increases from w, but to a lesser extent. The mean length scale calculated from the Fourier transform of the transverse velocity, $L_F^{u_y}$, remains close to the channel width, as expected, but shows increased fluctuations than in the lower activity states, representing the chaotic nature of the flows. These results are in accordance with Fig. S3 in the SI.

Since the wavelength of the waves excited in the channel flow varies from w to l (Fig. 4(a)), the characteristic length scales measured from the Fourier spectrum, $L_F^{u_x}$, $L_F^{u_y}$ and $L_F^{\omega_z}$, depend upon the channel length used in the simulations. Therefore it is helpful to also measure correlation lengths. $L_c^{u_x}$ (black), $L_c^{u_y}$ (red) and $L_c^{\omega_z}$ (yellow) corresponding to correlation functions of u_x, u_y and ω_z respectively (see SI, section S2.3, for exact definitions) are shown in Fig. 4(b).

In the oscillatory and dancing states, the correlation lengths corresponding to both components of the velocity field and the vorticity field remain the same, and are close to the channel width. In the localised active turbulent flow state, $L_c^{u_y}$ and $L_c^{\omega_z}$ are comparable to the channel width w while $L_c^{u_x}$ is slightly larger than w. Moreover, the standard deviations for the L_c are much smaller than those of the L_F.

Data showing how the length scales vary with the elastic constant K and the width of the channel w are presented in section S4 in the SI. We find that the vorticity correlation length, $L_c^{\omega_z}$, gives the clearest indication of the crossover from confined to bulk behaviour, which we discuss in more detail below.

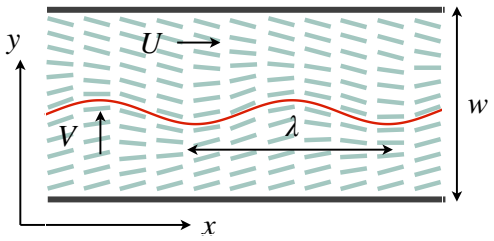

Fig. 5 Schematic illustrating the instability of the unidirectional flow field $U(y)\hat{x}$. The longitudinally (along the channel direction) perturbed director field is shown as dashed green lines. λ is the wavelength of the perturbation (red curve) and V is the transverse velocity generated by activity ζ that arises due to this perturbation. For small activity such perturbations do not persist but at higher activity, they grow and the flow turns oscillatory.

3.4 Instabilities generate flow transitions in confined active nematics

The existence of the multiple flow regimes discussed in the previous sections can be traced to the interplay between a cascade of instabilities and the confinement. In an unconfined, extensile active nematic, any long-range nematic order is unstable, and the system undergoes a cascade of bend instabilities, with successive instabilities having orthogonal wavevectors, which drive the flow state turbulent[52]. When the active nematic is confined, the confinement interrupts this natural instability mechanism leading to the different flow regimes:

No flow to unidirectional flow: In an active nematic, the first flow instability occurs when a bend instability forms across the channel[50].

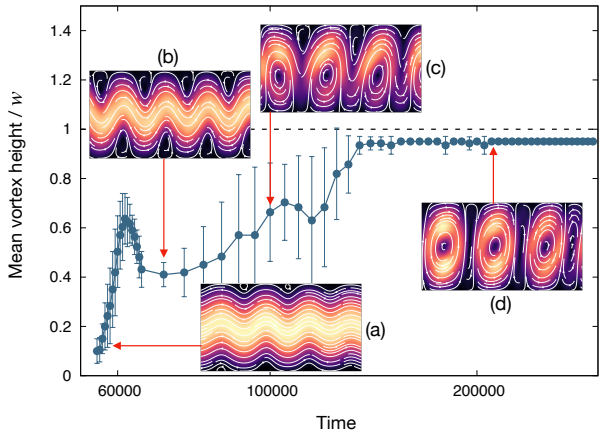

Fig. 6 Temporal increase of mean vortex height in a channel when the flow transitions from oscillatory flow to dancing flow. At steady state, in dancing flow, the vortex height saturates to w. Here the error bars indicate the standard deviation of the heights of all vortices present in the channel at a particular time. Four snapshots of the velocity field (a,b,c and d), corresponding to different time instances, are shown in the insets. The flow transition can be understood as the growth of waves in the velocity field (indicated by streamlines) in time. Once the amplitude of the waves becomes equal to the channel height the flow turns resulting in the dancing state.

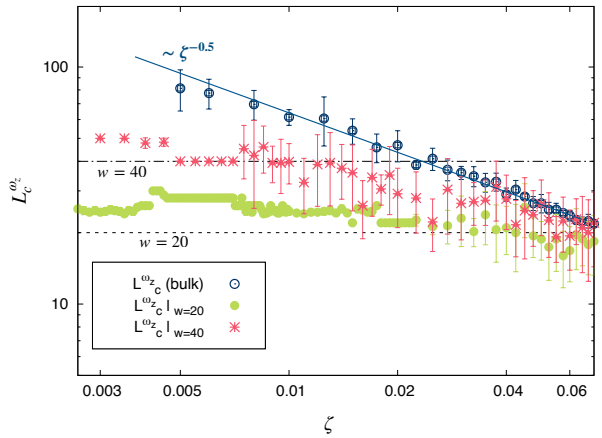

Fig. 7 Variation of the characteristic length $L_c^{\omega_z}$ obtained from the vorticity correlation functions for unconfined (dark blue) and confined, $w = 20$ (green) and $w = 40$ (red), active nematics.

Unidirectional flow to oscillatory flow: At higher activity, the unidirectional flows are unstable and bend instabilities along the channel arise in the director field. The wavelength selection mechanism in this transition can be understood by a scaling argument. Neglecting the elastic stress, and at low Reynolds number, eqn (2) becomes

$$\eta \nabla^2 \mathbf{u} - \zeta \nabla \cdot \mathbf{Q} = 0. \tag{4}$$

Consider a unidirectional flow, $\mathbf{u} = U(y)\hat{x}$, where the flow is entirely along the channel length with a close to parabolic flow profile as shown in Fig. 1(a). Linear stability analysis predicts that for unidirectional flows[50],

$$U \sim \frac{w\zeta q}{\eta}. \tag{5}$$

Further consider a longitudinal fluctuation in the director field of wavelength λ that generates a transverse component of velocity, V, as schematically illustrated in Fig. 5. The magnitude of this velocity is dictated by the active stress according to eqn (4) such that

$$\eta \frac{V}{\lambda^2} \sim \zeta \frac{q}{\lambda}. \tag{6}$$

However, the transverse velocity V is constrained by the equation of continuity $\nabla \cdot \mathbf{u} = 0$ and hence we have

$$\frac{U}{\lambda} \sim \frac{V}{w} \tag{7}$$

where w is the channel width, the natural length scale along the y-direction. Substituting for U from eqn (5) in eqn (7) and then using the resulting expression to eliminate V from eqn (6) we obtain

$$\lambda \sim w. \tag{8}$$

This argument demonstrates that the wavelength of the longitudinal perturbations that yield oscillatory flow state is w, the channel width. This agrees with the length scale obtained from our Fourier analysis, and explains results obtained in experiments and numerical simulations[30]. Note also that this secondary instability is similar to the observations in the experiment reported by Chandrakar et al.[34] where the instability wavelength is comparable to the channel width, but with the difference that the perturbations grow from a static nematic fluid in Chandrakar et al.[34], whereas the perturbations grow from a unidirectional flow stabilized director field in the scaling analysis above.

Oscillatory flow to dancing flow: A further increase in activity allows the transverse perturbation in the velocity field which gives rise to the oscillatory flow to grow but, as indicated by the Fourier analysis, the wavelength remains unchanged. When the amplitude of the wave becomes comparable to the channel width the flows turns back on itself to form the vortices which characterise the dancing state. This evolution is illustrated in Fig. 6 which plots the average vortex height in the channel as a function of time.

Dancing flow to localised active turbulence and to fully-developed turbulent flow: In a channel-confined active nematic the transition from the dancing state to fully-developed active turbulent flow occurs via the formation of local turbulent patches, termed active puffs[51], which can divide and decay in a process reminiscent of directed percolation in the space of channel length and time. The number of puffs, and their persistence in time, increase with increasing activity until they undergo a directed percolation transition to a connected state. The localised active turbulence state corresponds to a region where the puffs have started to form but do not percolate, the transition to fully-developed turbulence corresponds to the point where the puffs undergo the percolation

transition.

We showed, in sections 3.2 and 3.3 (see also section S5 in the SI), that the characteristic lengths in the localised active turbulence state are primarily determined by the channel width w. As the activity is increased, however, there is a crossover in behaviour which is most clearly seen in the vorticity correlation length, $L_c^{\omega_z}$. This transition is illustrated in Fig. 7 where we compare $L_c^{\omega_z}$ in channels of widths $w = 20$ and $w = 40$, and in an unconfined, bulk, system. The bulk correlation length decreases monotonically as $1/\sqrt{\zeta}$ as expected. The vorticity correlation length in the channel crosses over from w to the bulk value to follow the $L_c^{\omega_z}$ of the unconfined systems once the latter has dropped to w. This corresponds to the transition to the fully-developed turbulent state.

3.5 Active length scale and activity number

Typically, in the active turbulence literature, a single length scale, called the active length scale, is discussed[20,22,45]. The active length scale, which results from the competition between activity and elasticity, is taken to be $\sqrt{(K/\zeta)}$. It is a measure of the average size of a vortex or mean distance between defects. Our results make it clear that this definition is valid only in the bulk: in a channel-confined system length scales, such as the vortex size, are broadly set by the channel width but can also depend in detail on the way the characteristic length is defined.

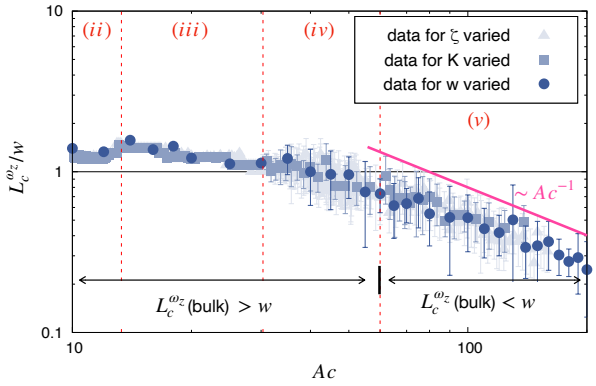

Fig. 8 Non-dimensionalised characteristic length scale based on ω_z is shown against the activity number Ac. The data is taken from Fig. 4, Figs. 7 and Fig. S4. Different symbols are used to distinguish different data sets: triangles are for variation in activity ζ, squares for variation in elasticity K and circles for variation in channel width w.

The existence of two length scales, the bulk active length scale and the channel width, mean that it is natural to define a non-dimensional number, the activity number[33,51,53], $Ac = w\sqrt{\zeta/K}$. Fig. 8 collects the data in Fig. 4, 7 and S4 together in a single plot of $L_c^{\omega_z}$ against activity number, showing a good data collapse and a clear crossover from confinement, where $L_c^{\omega_z}/w$ is independent of Ac, to bulk behaviour, where $L_c^{\omega_z}/w \sim Ac^{-1}$. The crossover occurs at $Ac \approx 55$.

The different flow regimes are indicated in Fig. 8. The flow transition from the unidirectional to the oscillatory state occurs at $Ac \approx 10$, the oscillatory to dancing transition occurs at $Ac \approx 13.5$ and the dancing to localised active turbulent flow transition occurs at $Ac \approx 30$. Throughout this range of activity numbers the length scale of the flow structures is equal to the channel width which underlines that confinement plays a decisive role in these transitions. In particular, the vortex-generating mechanism in the dancing flow is not the same as that of vortices occurring in the bulk.

4 Summary

We have investigated the dependence of the characteristic wavenumbers and lengths of channel-confined 2D extensile active nematic fluid flow on the fluid parameters and channel width. The characteristic lengths were derived by analyzing the field variables u_x, u_y and ω_z (components of velocity along and normal to the channel length, and the vorticity) associated with the flow field, using the most dominant Fourier mode from a discrete Fourier analysis and from the spatial correlation functions. Our analysis shows that the length scales are comparable to the channel width when the flow states are oscillatory or dancing. In the state of localised active turbulence, the characteristic length obtained from the Fourier transform ranges from the channel width w to the channel length l, while the correlation lengths remain comparable to the channel width w.

Our results emphasise that the active length scale is a *bulk* property. The physics of the confined states, oscillatory, dancing, and localised active turbulence, is set by the channel width. The crossover to fully-developed turbulence for increasing activity (or decreasing elasticity) occurs when the bulk active length scale decreases to the channel width.

Our findings are in accordance with previous experiments and simulations[9,30,35]. However we clarify that the flow transitions found in 2D confinement should not be interpreted as arising from a competition between confinement width and average vortex size. Rather we have argued here that the flow transitions result from various flow instabilities which dictate their characteristic lengths. In contrast to our result that the characteristic length associated with the confined flow states changes linearly with w, Hardoüin *et al.* [30] report a $\sim \sqrt{w}$ dependence. This difference seems to arise because in the latter work the data from both fully developed turbulence and other states were fitted to a single curve.

To summarise the dependence of the length scales on fluid parameters activity (ζ), elasticity (K) and channel width (w), we plot the non-dimensionalised vorticity correlation length $L_c^{\omega_z}/w$ against activity number $Ac = w\sqrt{\zeta/K}$ in Fig. 8. All data points collapse well to a single curve. When $Ac \lessapprox 55$, $L_c^{\omega_z}$ scales with the channel width w whereas for $Ac \gtrapprox 55$, which correspond to fully-developed turbulent flows, $L_c^{\omega_z}/w$ scales as Ac^{-1} indicating a crossover to behaviour controlled by the bulk active length scale. Thus there is a critical activity number for channel-confined active nematic fluids, below which the physics of the flow structures is dictated by the confinement, and above which the flow is that of an unconfined system.

Conflicts of interest

There are no conflicts to declare.

Acknowledgements

We acknowledge Manoj Gopalakrishnan and Santhan Chandragiri for very helpful discussions during this work. We also thank HPCE, IIT Madras for high performance computing facilities.

Notes and references

1 S. Ramaswamy, *Annu. Rev. Condens. Matter Phys.*, 2010, **1**, 323–345.

2 M. C. Marchetti, J.-F. Joanny, S. Ramaswamy, T. B. Liverpool, J. Prost, M. Rao and R. A. Simha, *Rev. Mod. Phys.*, 2013, **85**, 1143.

3 M. J. Bowick, N. Fakhri, M. C. Marchetti and S. Ramaswamy, *arXiv:2107.00724*, 2021.

4 C. Bechinger, R. Di Leonardo, H. Löwen, C. Reichhardt, G. Volpe and G. Volpe, *Rev. Mod. Phys.*, 2016, **88**, 045006.

5 C. Dombrowski, L. Cisneros, S. Chatkaew, R. E. Goldstein and J. O. Kessler, *Phys. Rev. Lett.*, 2004, **93**, 098103.

6 H. H. Wensink, J. Dunkel, S. Heidenreich, K. Drescher, R. E. Goldstein, H. Löwen and J. M. Yeomans, *Proc. Natl. Acad. Sci. U.S.A.*, 2012, **109**, 14308–14313.

7 A. Sokolov and I. S. Aranson, *Phys. Rev. Lett.*, 2012, **109**, 248109.

8 D. Nishiguchi, K. H. Nagai, H. Chaté and M. Sano, *Phys. Rev. E*, 2017, **95**, 020601.

9 H. Wioland, E. Lushi and R. E. Goldstein, *New J. Phys.*, 2016, **18**, 075002.

10 S. R. K. Vedula, M. C. Leong, T. L. Lai, P. Hersen, A. J. Kabla, C. T. Lim and B. Ladoux, *Proc. Natl. Acad. Sci. U.S.A.*, 2012, **109**, 12974–12979.

11 A. Doostmohammadi, S. P. Thampi, T. B. Saw, C. T. Lim, B. Ladoux and J. M. Yeomans, *Soft Matter*, 2015, **11**, 7328–7336.

12 K. Kawaguchi, R. Kageyama and M. Sano, *Nature*, 2017, **545**, 327–331.

13 Y. Sumino, K. H. Nagai, Y. Shitaka, D. Tanaka, K. Yoshikawa, H. Chaté and K. Oiwa, *Nature*, 2012, **483**, 448–452.

14 T. Sanchez, D. T. N. Chen, S. J. DeCamp, M. Heymann and Z. Dogic, *Nature*, 2012, **491**, 431–434.

15 V. Narayan, S. Ramaswamy and N. Menon, *Science*, 2007, **317**, 105–108.

16 N. Kumar, H. Soni, S. Ramaswamy and A. K. Sood, *Nat. Commun.*, 2014, **5**, 4688.

17 M. E. Cates and J. Tailleur, *Annu. Rev. Condens. Matter Phys.*, 2015, **6**, 219–244.

18 J. Dunkel, S. Heidenreich, K. Drescher, H. H. Wensink, M. Bär and R. E. Goldstein, *Phys. Rev. Lett.*, 2013, **110**, 228102.

19 V. Bratanov, F. Jenko and E. Frey, *Proc. Natl. Acad. Sci. U.S.A.*, 2015, **112**, 15048–15053.

20 P. Guillamat, J. Ignés-Mullol and F. Sagués, *Nat. Commun.*, 2017, **8**, 564.

21 S. P. Thampi, R. Golestanian and J. M. Yeomans, *Europhys. Lett.*, 2014, **105**, 18001.

22 L. Giomi, *Phys. Rev. X*, 2015, **5**, 031003.

23 E. J. Hemingway, P. Mishra, M. C. Marchetti and S. M. Fielding, *Soft Matter*, 2016, **12**, 7943–7952.

24 M. M. Norton, A. Baskaran, A. Opathalage, B. Langeslay, S. Fraden, A. Baskaran and M. F. Hagan, *Phys. Rev. E*, 2018, **97**, 012702.

25 A. Opathalage, M. M. Norton, M. P. N. Juniper, B. Langeslay, S. A. Aghvami, S. Fraden and Z. Dogic, *Proc. Natl. Acad. Sci. U.S.A.*, 2019, **116**, 4788–4797.

26 K. Suzuki, M. Miyazaki, J. Takagi, T. Itabashi and S. Ishiwata, *Proc. Natl. Acad. Sci. U.S.A.*, 2017, **114**, 2922–2927.

27 F. C. Keber, E. Loiseau, T. Sanchez, S. J. DeCamp, L. Giomi, M. J. Bowick, M. C. Marchetti, Z. Dogic and A. R. Bausch, *Science*, 2014, **345**, 1135–1139.

28 P. W. Ellis, D. J. G. Pearce, Y.-W. Chang, G. Goldsztein, L. Giomi and A. Fernandez-Nieves, *Nat. Phys.*, 2018, **14**, 85–90.

29 K.-T. Wu, J. B. Hishamunda, D. T. N. Chen, S. J. DeCamp, Y.-W. Chang, A. Fernández-Nieves, S. Fraden and Z. Dogic, *Science*, 2017, **355**, eaal1979.

30 J. Hardoüin, R. Hughes, A. Doostmohammadi, J. Laurent, T. Lopez-Leon, J. M. Yeomans, J. Ignés-Mullol and F. Sagués, *Commun. Phys.*, 2019, **2**, 121.

31 M. Varghese, A. Baskaran, M. F. Hagan and A. Baskaran, *Phys. Rev. Lett.*, 2020, **125**, 268003.

32 S. Chandragiri, A. Doostmohammadi, J. M. Yeomans and S. P. Thampi, *Phys. Rev. Lett.*, 2020, **125**, 148002.

33 T. N. Shendruk, A. Doostmohammadi, K. Thijssen and J. M. Yeomans, *Soft Matter*, 2017, **13**, 3853–3862.

34 P. Chandrakar, M. Varghese, S. A. Aghvami, A. Baskaran, Z. Dogic and G. Duclos, *Phys. Rev. Lett.*, 2020, **125**, 257801.

35 Y. Fan, K.-T. Wu, S. A. Aghvami, S. Fraden and K. S. Breuer, *Phys. Rev. E*, 2021, **104**, 034601.

36 T. Strübing, A. Khosravanizadeh, A. Vilfan, E. Bodenschatz, R. Golestanian and I. Guido, *Nano Lett.*, 2020, **20**, 6281–6288.

37 P. D. Olmsted and P. M. Goldbart, *Phys. Rev. A*, 1992, **46**, 4966.

38 G. Tóth, C. Denniston and J. M. Yeomans, *Phys. Rev. Lett.*, 2002, **88**, 105504.

39 C. Denniston, G. Tóth and J. M. Yeomans, *J. Stat. Phys.*, 2002, **107**, 187–202.

40 R. A. Simha and S. Ramaswamy, *Phys. Rev. Lett.*, 2002, **89**, 058101.

41 Y. Hatwalne, S. Ramaswamy, M. Rao and R. A. Simha, *Phys. Rev. Lett.*, 2004, **92**, 118101.

42 D. Marenduzzo, E. Orlandini, M. E. Cates and J. M. Yeomans, *Phys. Rev. E*, 2007, **76**, 031921.

43 A. N. Beris and B. J. Edwards, *Thermodynamics of flowing systems: with internal microstructure*, Oxford Univ. Press, 1994.

44 S. Santhosh, M. R. Nejad, A. Doostmohammadi, J. M. Yeomans and S. P. Thampi, *J. Stat. Phys.*, 2020, **180**, 699–709.

45 S. P. Thampi, R. Golestanian and J. M. Yeomans, *Phil. Trans. R. Soc. A*, 2014, **372**, 20130366.
46 S. P. Thampi, R. Golestanian and J. M. Yeomans, *Phys. Rev. Lett.*, 2013, **111**, 118101.
47 C. Denniston, E. Orlandini and J. M. Yeomans, *Phys. Rev. E*, 2001, **63**, 056702.
48 M. E. Cates, S. M. Fielding, D. Marenduzzo, E. Orlandini and J. M. Yeomans, *Phys. Rev. Lett.*, 2008, **101**, 068102.
49 O. Henrich, K. Stratford, D. Marenduzzo and M. E. Cates, *Proc. Natl. Acad. Sci. U.S.A.*, 2010, **107**, 13212–13215.
50 R. Voituriez, J.-F. Joanny and J. Prost, *Europhys. Lett.*, 2005, **70**, 404–410.
51 A. Doostmohammadi, T. N. Shendruk, K. Thijssen and J. M. Yeomans, *Nat. Commun.*, 2017, **8**, 15326.
52 B. Martínez-Prat, J. Ignés-Mullol, J. Casademunt and F. Sagués, *Nat. Phys.*, 2019, **15**, 362–366.
53 S. Chandragiri, A. Doostmohammadi, J. M. Yeomans and S. P. Thampi, *Soft Matter*, 2019, **15**, 1597–1604.